Mech. Adv. Technol., Vol. 9, No. 4, 2025, pp. 483–494

DOI: 10.20535/2521-1943.2025.9.4(107).345010

UDK 621.9.048.74

Integrated Geometric Confinement and Ejection-Driven Drainage Flow for Splash Suppression in High-Speed Abrasive Waterjet Machining

Xianding Xue[1] - ORCID https://orcid.org/0009-0004-5909-1573
Oleksandr Salenko[1] - ORCID https://orcid.org/0000-0002-5685-6225

Received: 17 September 2025 / Revised: 1 December 2025 / Accepted: 24 December 2025

Abstract: *Abrasive waterjet machining (AWJM) is widely used in aerospace and precision manufacturing due to its cold-cutting nature. However, the residual high-energy jet column penetrating the workpiece frequently impacts the support structure, generating intense splashback that leads to surface contamination and secondary damage. To address this, we propose a composite anti-splash support structure integrating a concave bowl surface with a Venturi-induced negative pressure mechanism. Using VOF multiphase modeling combined with finite element validation, we elucidate the synergistic control mechanism: the curved bowl promotes wall-adherent liquid sliding to reduce radial momentum, while the Venturi throat creates a ~0.15 MPa negative pressure zone that captures droplets into the downstream channel for dissipation. Results demonstrate that compared to conventional supports, the design reduces mixture peak velocity by ~35 %, decreases droplet diffusion height by 40 %, and curtails radial spread by 30 %, effectively constraining contamination areas. Static analysis further confirms the structure maintains high safety margins even under extreme loads. These outcomes not only enhance AWJM processing environments but also provide a validated engineering paradigm for high-speed fluid interaction control. Looking forward, the mechanism resonates with splash suppression needs in photolithography, food packaging, electronic encapsulation, and metal cutting, paving the way for a universal design and evaluation system for splash control in advanced manufacturing.*

Keywords: *Abrasive waterjet machining; Splash suppression; Venturi effect; Numerical simulation; Fluid-structure interaction.*

Introduction

Abrasive waterjet machining (AWJM) as a cold-cutting technology has found extensive applications in aerospace, railway transportation, and precision manufacturing [1], [2]. It is particularly suitable for thermally sensitive and difficult-to-machine materials such as polymers and carbon fiber reinforced plastics (CFRP) [3]. However, a long-standing and unresolved problem in AWJM is the formation of high-energy residual liquid jets after workpiece penetration [4]. This liquid column impacts the underlying support structure, causing intense splashback that subsequently contaminates or damages already processed surfaces.

Conventional abrasive waterjet processing is typically implemented when cutting sheet materials mounted on worktable supports. These supports are generally designed as knife-edge structures, consisting of sufficiently thin plates (typically 1.5–2.5 mm) mounted vertically, which represent rapidly wearing elements. During each cutting operation, when the cutting jet passes over such supports, a short-term high-intensity reverse flow with alternating directions is formed, capable of causing damage to the back side of the workpiece. Periodic surface waves from the reverse fluid action are sometimes observed [5], [6], particularly when processing low-strength workpieces.

Hazard of Splash and the Necessity of Control

Previous studies have demonstrated that post-penetration splash is not merely liquid dispersion but contains abrasive particles with residual kinetic energy, high-speed disturbed airflow, and fragmented liquid film debris. These factors collectively can cause severe problems on the workpiece's lower surface and surrounding equipment [1], [7], [8]:

– Surface quality degradation: Splash droplets cause micro-defects including erosion, fiber fracture, and edge resin loss.

[1] *National Technical University of Ukraine "Igor Sikorsky Kyiv Polytechnic Institute", Ukraine, Kyiv, Ukraine https://ror.org/00syn5v21*

✉ *Xianding Xue xiandingx@gmail.com*

– Abrasive embedding: High-energy particles rebound to the workpiece backside during splash. In resin-softened zones or interfacial delamination areas, they may become embedded in the material, leading to interlaminar strength reduction and surface peeling.

– Unpredictable contamination zones: Splash severity is highly stochastic, depending on flow disturbances and support structure geometry, making parameter adjustment ineffective as a preventive measure.

– Operational inconvenience: Conventional support structures (e.g., mesh or groove supports) struggle to precisely align jet penetration paths with bottom cavities, resulting in residual jets directly impacting metal support rods and exacerbating splash formation.

The high pressure for generating high-velocity fluid jets is provided by a hydraulic intensifier system coupled with an accumulator, capable of smoothing periodic pressure fluctuations during intensifier switching [9]. This achieves relative process stability; however, surface defect formation occurs beyond the hydraulic erosion zone. Such phenomena are evidenced by studies [10], [11] where authors attempt to avoid such damage during test specimen preparation. One proposed solution involves fundamentally redesigning the waterjet machine layout where the abrasive-jet system remains stationary while the workpiece moves [12]. The significant drawback of this system is the requirement for rigid clamping elements and potential limitations in jet system trajectory and cut geometry, which may be negligible given high stability and processing quality requirements.

Therefore, solving the problem of uncontrolled splash contamination and lack of protective structures requires developing support structures with precise geometric control and flow guidance mechanisms. Such structures should achieve dual objectives of splash trajectory convergence and residual energy dissipation.

Research Objective and Approach

To mitigate splash formation, this study proposes a hybrid anti-splash support structure with two key design innovations:

– Concave bowl geometry: this feature confines the residual liquid jet and constrains the initial splash angle

– Venturi-effect ejection channel: by injecting 1.6 MPa compressed air, the channel creates a low-pressure suction zone through flow ejection, establishing an “adsorption-dispersion-extraction” control mechanism.

Research Foundation Materials

1. Theoretical Background

The authors [13] investigated the physical phenomena of material wear by abrasive particle flow during hydro-abrasive machining, analyzing the process of single-particle impact on surfaces leading to crater formation. Studies of craters [14] formed by particle impacts at various attack angles revealed that material displaced from the crater flows along the particle impact direction, forming ridges until fracture occurs due to significant high-rate accumulated deformations. For 90° impacts, ridges distribute uniformly around the crater periphery, while at lower attack angles, ridges form preferentially along the crater sides and particle trajectory. The deformation characteristics [15] depend on particle shape, orientation upon surface contact, impact velocity, impact angle, and the material properties of both abrasive and target surfaces.

In abrasive waterjet machining, abrasive particles interact with the workpiece surface within a liquid medium that envelops the particles and penetrates directly into the contact zone, inducing material removal. This process continuously evacuates machining debris from the cutting kerf. The abrasive mixture consists of water mixed with fine abrasive particles (e.g., garnet sand averaging 0.4 mm in size, composed primarily of Al_2O_3 corundum, SiO_2 quartz, Fe_2O_3 iron oxide, and other components). The cutting tool – the abrasive mixture – simultaneously functions as a coolant. According to [16], thermally induced structural changes in the material surface layer cannot occur under these conditions, confirming that hydro-abrasive cutting constitutes a cold mechanical material removal process.

In work [17], the explanation of surface damage by abrasive particles considers the physico-mechanical properties of both abrasive and workpiece materials, abrasive particle geometry, the ratio of penetration depth to particle tip radius (h/r), and destructive forces. Three material removal mechanisms are identified:

– In this regime where $h/r < 0.01$ (where h = penetration depth in mm, r = abrasive grain tip radius in mm), material removal occurs through frictional contact fatigue mechanisms.

– Polydeformational failure (plastic contact): h/r = = 0,01...0,5;

– Micro-cutting (brittle and ductile fracture): this removal mechanism occurs at large cutting angles and h/r ratios > 0.5. Since abrasive particles possess irregular shapes and may assume random spatial orientations during impact, the deformation processes within the contact zone remain non-uniform even under constant attack angles, velocities, and abrasive particle masses.

The general schematic of the hydro-abrasive cutting setup is illustrated in Fig. 1 according to.

Here, h_{op} – free jet path length; $D_к \approx b_r$ – kerf width; d_s – nozzle diameter; α – liquid outflow angle, i.e., the angle between the direction of movement without cutting and the outflow direction; q_b – fluid flow rate in the nozzle; M_a – mass of abrasive.

High-pressure water (400 MPa and above), generated by a high-pressure pump, passes through a jet nozzle forming a jet with a diameter of d_s = 0.2–0.35 mm, and enters the mixing chamber. In the mixing chamber, water is mixed with abrasive; subsequently, the mixture passes

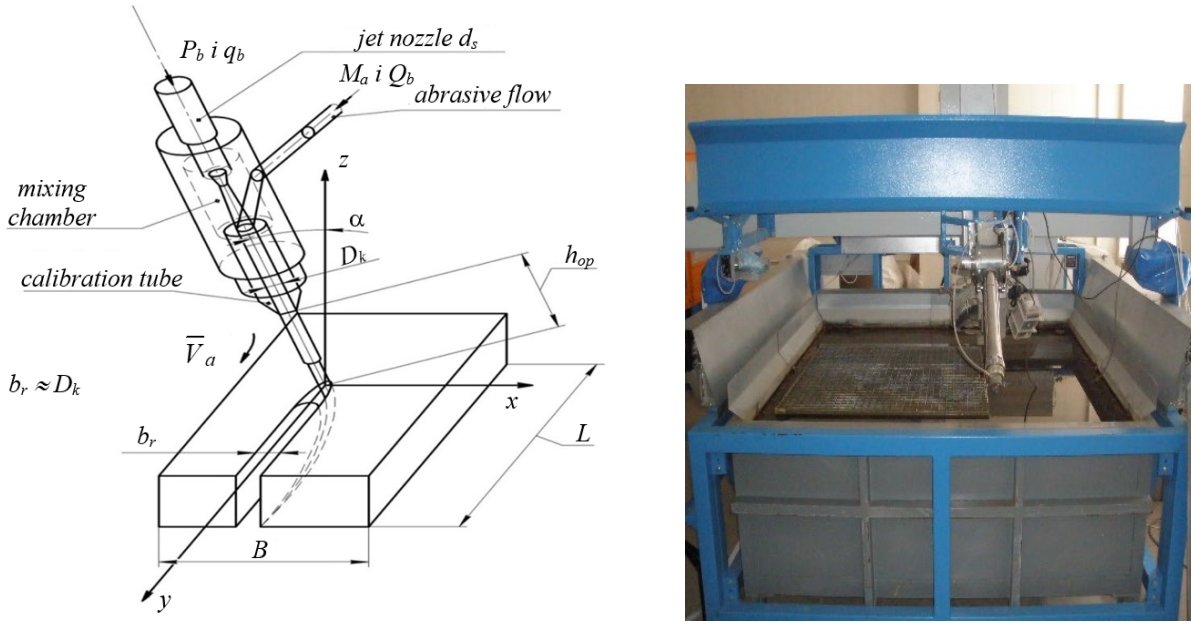

Fig. 1. Schematic diagram of hydro-abrasive cutting setup and waterjet cutting machine

through a second nozzle made of hard alloy or diamond with an internal diameter of D_k = 0.6–1.2 mm. From this nozzle, the water–abrasive jet exits at a velocity of approximately 1000 m/s and impinges on the surface of the material being cut.

In works [17], the authors investigated the characteristics of abrasive water jet cutting and demonstrated that material removal under an abrasive water jet occurs through two mechanisms: mechanical wear (or micro-cutting processes by individual abrasive particles) resulting from the impacts of abrasive grains impinging on the processed surface at small angles, and deformation wear resulting from the impacts of particles striking the surface at significantly larger angles.

The first cutting mechanism leads to a cut surface with a uniformly distributed depth, while the second results in a surface with a non-uniformly distributed depth. It is also considered that the relative contribution of each mechanism to the total cutting depth depends on the feed rate. Cutting is realized solely due to deformation wear when the feed rate exceeds a certain threshold value. The simplified formula proposed by the authors [18] for determining the cutting depth h is as follows:

$$h = c\sqrt{\frac{m_a v^2}{8\sigma u}} + \frac{2m_a(1-c)v^2}{\pi u \varepsilon d_j}$$

The first term of the presented equation defines mechanical destruction, while the second corresponds to deformation destruction. The critical value of the feed rate u, at which the deformation destruction mechanism becomes predominant and mechanical destruction is almost absent, is proposed to be determined by the following formula:

$$u_c \equiv \frac{m_a v^2}{20\sigma d_j^2}$$

The authors of work proposed to describe the process of abrasive water jet cutting by comparing the energy of the abrasive water jet with the fracture energy of the solid body:

$$N = \frac{1}{2}\left(f_b\sqrt{2p_b\rho} + M_a\right)\left(\frac{2p_b f_b}{f_b\sqrt{2p_b\rho} + M_a}\right)$$

For the simplification of the mathematical description, the researchers adopted a number of assumptions, the main ones being as follows: the jet is absolutely rigid, undeformed, and its cross-section is circular; the position of the jet axis relative to the workpiece remains unchanged throughout the entire time of fracture of the control volume; the velocity distribution across the jet cross-section is uniform and depends on the distance from the nozzle exit; the abrasive particles are uniformly distributed over the jet cross-section, their mass m_a is identical and equal to the average mass of the fraction; the strength of the material is constant, and the material is homogeneous; external disturbances are absent.

In work [19], the author obtained a model of the kinetics of particle motion and of the flow as a whole in the cutting performance problem, which is universal and therefore can be used for optimization calculations, since it takes into account a number of factors of the technological system.

According to the concept of M. Hashish, two zones can be distinguished through the thickness of the material being cut. In the region on the jet entrance side, material is

removed as a result of the micro-cutting mechanism of the jet action with an attack angle close to 90°. With the degree of jet penetration into the depth of the material, the attack angle changes, the jet loses power, and grooves are formed on the cutting plane at the jet exit side. At this stage, the erosion mechanism is based on deformation wear. The second zone is characterized by grooves and waviness of the surface.

The analysis of the distribution of kinetic energy across the flow cross-section and the assessment of the fracture work performed by an individual abrasive particle was proposed in work [20] by O. F. Salenko and O. V. Fomovska.

It was shown that cutting (with progressive feed) occurs under quasi-steady conditions, i.e., during cutting, the conditions of interaction between the jet and the workpiece do not change. Fig. 2 shows the scheme of cutting straight sections.

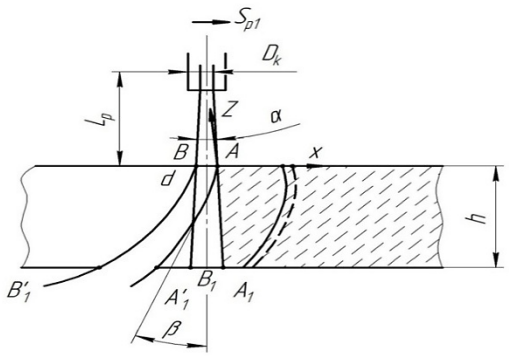

Fig. 2. Scheme of cutting straight sections

Here, Sp_1 – direction of progressive feed; D_k – diameter of the calibration tube; α – jet expansion angle $AB = f(L_p, \alpha)$, where AB is the cross-sectional dimension on the processing surface; A'_1, B'_1 – jet dimension formed when enveloping the groove front of the cut; β – averaged jet deflection angle, which depends on the cutting conditions of the material with thickness h; A'_1 – the envelope (front) of the cutting groove, which will be subjected to hydrodynamic impact.

Complete or incomplete penetration is determined by the ratio of the working feed rate to the jet penetration rate into the material. The penetration rate, in turn, is defined by the physico-mechanical properties of the material, the so-called machinability. It should be noted that although different materials possess different strength, stiffness, and machinability parameters, machinability is not unequivocally determined by these characteristics. It is known that more brittle and stiffer materials exhibit better machinability. Therefore, for the calculation of material removal volume (Fig. 3) or working feed rate, several mathematical descriptions are applied, which are presented in the literature, in particular:

$$w_i = \frac{M_a}{m_a} w_s ,$$

where M_a – mass flow rate of abrasive; m_a – mass of an abrasive particle; M_a/m_a – number of interaction acts; $w_s = \frac{\pi \dot{x}_a^2 (3R_a - x_a)}{3}$, where w_s – volume of material removed in one act of interaction; w_i – volume of material removed per unit time; $\dot{x}_a$ – particle velocity $\left(\dot{x}_a = \frac{dx_a}{dt} \right)$; R_a – radius of the abrasive particle; x_a – position of the abrasive particle relative to the surface; $\vec{V}_a$ – penetration velocity into the material; V_p – total particle velocity, determined on the basis of the energy balance at the particle exit from the nozzle.

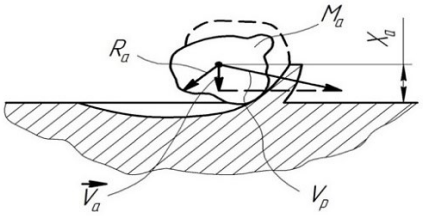

Fig. 3. Deformation–wear phenomena during the contact of an abrasive particle with the material surface

Thus, even after passing beyond the boundaries of the processed workpiece, the jet–abrasive flow is still capable of performing fracture work and, as a consequence, causing damage to the workpiece.

From a technological perspective, the use of abrasive in the cutting process leads to intensive wear of the nozzle head (the hard-alloy tube or the mixing chamber as a whole), which results in its frequent replacement and increases the cutting cost. The quality of the edge obtained by abrasive water jet cutting also deteriorates.

Such damage, Fig. 4, is caused both by the formation of reverse fluid flow when it impinges on the support structure of the table and by splashing of the jet containing abrasive particles.

Fig. 4 illustrates a typical example of damage caused by splashing along the edges of a CFRP workpiece. The red regions highlight edge erosion and material delamination induced by the reverse splash flow.

Unlike the aforementioned works, the authors consider the formation of the surface and the geometry of the final product taking into account the following features:

– Modeling of splash formation and development phenomena using a multiphase Volume of Fluid (VOF) model;

– Designing of an anti-splash protection structure and constructing a comparative baseline model to verify suppression efficiency;

– Performing static analysis to confirm structural stability under typical loading conditions;

– Assessing protective capability through visualization of trajectories, volume fraction fields, and contamination zone mapping

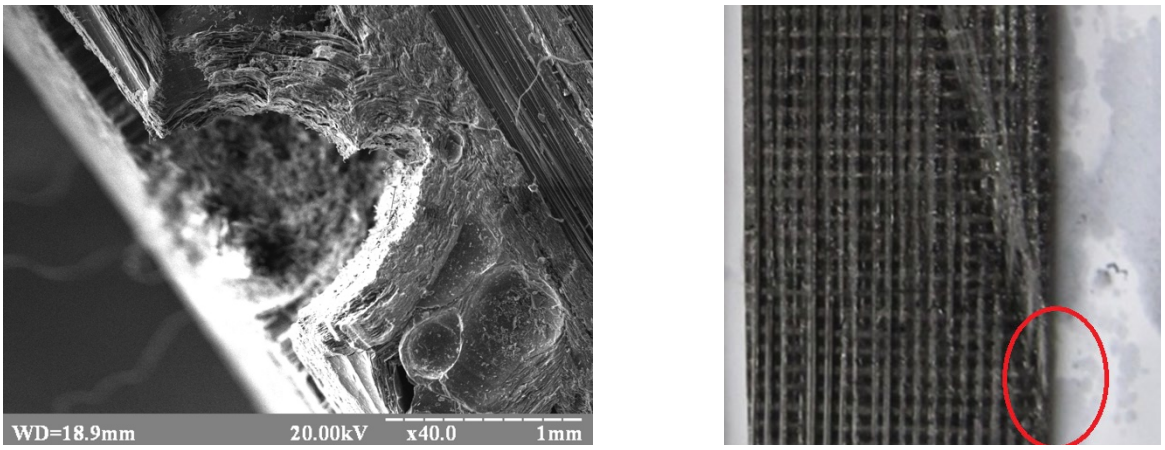

a *b*

Fig. 4. Damaged reverse surface (*a*) and the effect of the draining fluid flow by end surface (*b*)

2. Applied design

The theoretical background lies in the fact that the mass flow rate of abrasive particles introduced into the jet stream due to air ejection in the mixing chamber is determined by the jet outflow conditions and the geometrical parameters of the nozzle, chamber, and abrasive feeding tube. Based on the Mendeleev–Clapeyron equation, the mass flow rate of abrasive particles has been established as a function of the geometrical parameters of the jet-forming system, kg/min:

$$Q_m = \frac{5}{2}\mu\pi d_c^{\,2}\sqrt{\frac{2p_b d_j^2 l_j \rho_r}{\left[x_a\rho_r + \rho_a\left(100 - x_a\right)\right]d_k^2 l_k}},$$

where d_c, d_j, d_k – diameters of the nozzle, orifice jet, and mixing chamber, respectively, m; μ – nozzle discharge coefficient; ρ_a, ρ_r – density of abrasive particles and liquid, respectively, kg/m^3; l_j, l_k – length of the orifice jet and mixing chamber, respectively, m; χ_a – mass concentration of abrasive in the liquid, %; p_b – jet outflow pressure, Pa.

Similar considerations regarding the ejection of the flow under high-velocity liquid motion in a constricted cross-section, known as the Venturi effect, can also be applied to a design in which a high-speed transverse flow is used to suppress and straighten the draining liquid flow that has already performed the cutting work on the workpiece.

The design consists of a three-section coaxial configuration (Fig. 5 *a*) with specially tuned inlet and outlet openings for the liquid:

– Upper convergence zone (concave bowl surface): After penetrating the workpiece, the liquid jet enters the bowl region. The axisymmetric concave surface forces the jet to glide along the inner wall, forming an attached liquid film. This substantially reduces radial momentum and delays edge instabilities of the liquid rim. Annular drainage holes are distributed along the rim of the bowl, allowing part of the liquid to be discharged earlier and preventing excessive thickening and instability of the film. Fig. 5 *b* shows the internal structure of the bowl, where the central main outlet and annular drainage holes (with diameters larger than typical abrasive particles) work synergistically to achieve stepwise discharge and reconvergence.

– Middle buffer cavity: The liquid collected by the bowl drains into a T-shaped cavity, where initial dispersion and dissipation of kinetic energy occur. This region also acts as a gas–liquid interaction zone, providing stable inlet conditions for the negative pressure field generated by the downstream Venturi channel.

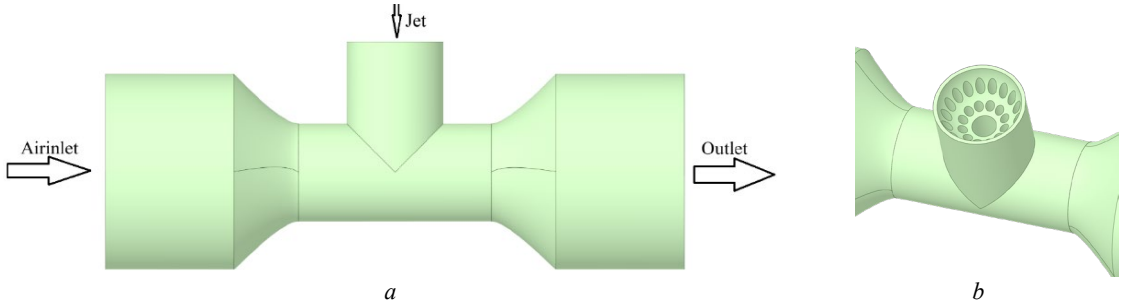

a *b*

Fig. 5. Overall structure and functional segmentation (*a*) and internal structure of the concave bowl (*b*)

– Lower Venturi induction zone: In the contraction–throat–expansion channel, compressed air at a pressure of 1.6 MPa is introduced laterally. As the gas accelerates through the throat to several hundred meters per second (approximately 400–600 m/s), a significant drop in static pressure is generated (negative pressure of about 0.15 MPa). This suction effect acts on the liquid film inside the cavity, continuously drawing droplets and films toward the throat and carrying them along with the air stream. Ultimately, the gas–liquid mixture is smoothly released through the downstream expansion section into the external collection system, forming a closed-loop flow.

Thus, the proposed design can be seamlessly integrated into real processing platforms, offering both a clear theoretical justification and practical feasibility.

The mechanism and implementation of suppression are achieved through the following solutions.

Geometric constraint of the concave bowl: the curvature of the bowl, aided by drainage holes, forces the jet to transition into a wall-attached flow, delaying Kelvin–Helmholtz instabilities and rim breakup, thereby suppressing primary splashing.

Aerodynamic induction: Venturi throat: Lateral injection of compressed air is accelerated through the throat, generating a negative pressure field. This suction continuously draws films and droplets downward into the channel, preventing upward dispersion.

Workpiece interface and flow direction: the upper flange maintains a minimal clearance with the backside of the workpiece, ensuring immediate entry of the penetrated jet into the bowl region. Meanwhile, compressed air enters the throat laterally, entraining droplets into the downstream expansion section. The gas–liquid mixture is eventually discharged into external systems for mist removal and collection, ensuring no adverse effects on processing quality or environmental cleanliness.

The structural housing is manufactured from 304 stainless steel with a yield strength of approximately 215 MPa and a tensile strength of about 505 MPa. This material offers excellent corrosion resistance and machinability. Considering the operating conditions in this study, it meets the strength and durability requirements without the need for additional coatings, such as tungsten carbide.

Taking as a basis a carbon fiber plate with a thickness of 3 mm, approximately 25 support points distribute the load per square meter. The actual load per support point is about 2.53 N, which was amplified 100 times to 253 N for the analysis of extreme conditions. In the finite element configuration, fixed boundaries were applied at the junction between the support and the external platform, while the concentrated load was placed on the flange of the bowl. The transition regions and throat areas were locally refined in the mesh to improve stress resolution.

– Equivalent stress (von Mises): the maximum stress was about 8.08 MPa (Fig. 6 *a*), concentrated in the Venturi throat region and bowl transition, which is significantly lower than the yield strength of 304 stainless steel. The safety factor is approximately 26.6.

– Equivalent strain: the maximum strain was 4.33×10^{-5} (Fig. 6 *b*), with displacements less than 5 μm, which is negligible in terms of influencing the induction effect of the flow in the bowl and throat.

The results confirm that even under amplified extreme loading, the structure retains a large margin of strength and stability, ensuring reliable long-term service and providing a solid basis for further studies of the splash suppression mechanism.

For comparison, the baseline support structure was developed based on conventional configurations. Unlike the proposed system, this design does not include either the bowl-shaped convergence surface or the Venturi-induced suction channel. Instead, it relies solely on gravitational drainage and a limited channel-guided flow.

The orthogonal frame represents, Fig. 7, a traditional drainage support structure, where the upper surface directly supports the workpiece during cutting. At its cen-

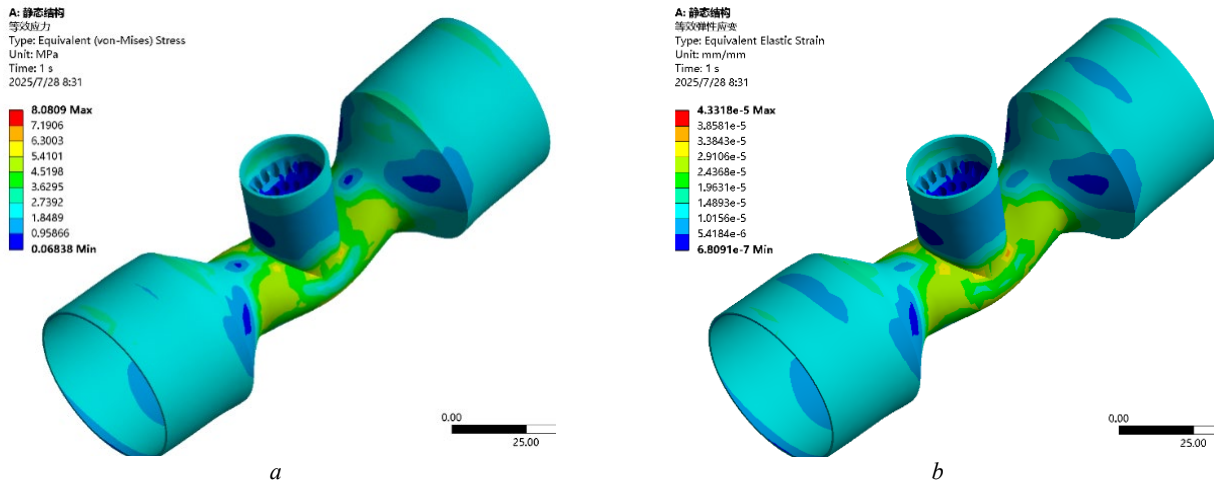

a *b*

Fig. 6. Distribution of equivalent stresses (*a*) and distribution of equivalent strains (*b*)

ter, a cylindrical cavity encompasses the area corresponding to the already processed surface, serving as a volume in which splash behavior is assessed. This cavity element is also present in the experimental structure with identical dimensions, ensuring that the differences observed in Section 4 can be attributed exclusively to the presence or absence of splash-protection elements.

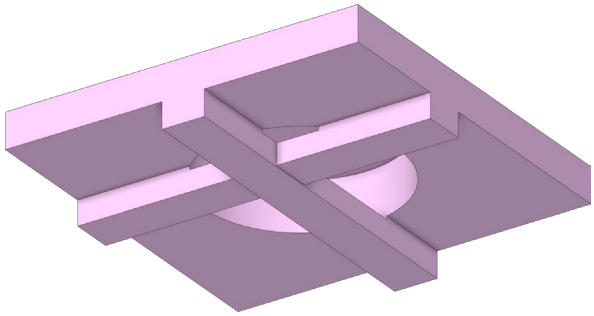

Fig. 7. Scheme of the baseline support structure

3. Numerical modeling and its configuration

In this study, numerical modeling was applied to analyze the flow and pressure characteristics of the proposed anti-splash design under typical abrasive water jet machining (AWJM) conditions, thereby confirming the effectiveness and mechanistic justification of the design. Numerical modeling enables detailed observation of flow field behavior without the cost of physical experiments and allows systematic evaluation of how structural parameters affect flow dynamics, providing scientific recommendations for further optimization. The reliability of the modeling depends on the adoption of appropriate physical models, governing equations that meet the requirements, boundary conditions, grid-independence verification, and consistency with theoretical calculations.

3.1 Multiphase flow model and governing equations

Considering the strong interaction between high-speed water and air phases in AWJM, the Volume of Fluid (VOF) multiphase model was selected to track the gas–liquid interface and accurately capture droplet motion and aerodynamic induction phenomena. The governing equations solved include the continuity equation for incompressible fluids, the momentum conservation equations, and the phase fraction transport equation, with a stochastic k–ε turbulence model introduced to describe high-speed turbulent characteristics. This system of equations effectively reflects the pressure fluctuations and velocity distribution of the high-speed multiphase flow in the contraction–expansion channel and concave cavity, thereby providing a reliable theoretical basis for splash suppression analysis.

Numerical model and observation planes for the anti-splash design given on the Fig. 8.

For ensuring stability and accuracy, the transient pressure–velocity coupling was achieved using the PISO algorithm, while surface tension effects were represented by the Continuous Surface Force (CSF) model. The time step was strictly controlled so that the Courant number remained below 0.25, which corresponds to the established stability criteria for free-surface flows. The level of negative pressure in the Venturi region (approximately 0.15 MPa), calculated by Bernoulli's equation, was consistent with the simulation results, further confirming the physical validity of the model.

3.2 Geometry, boundary conditions, and observation surfaces

The computational domain was based on the anti-splash structure described in Section 2, retaining the primary flow regions while simplifying peripheral details to reduce computational cost without compromising key physical processes. The boundary conditions were chosen as follows:

– High-pressure water inlet (400 MPa, outlet velocity ≈ 632 m/s): this pressure level corresponds to standard industrial practice of AWJM, reproducing the high energy density of the jet and its impact on the support structure.

– High-pressure air inlet (1.6 MPa, creating ≈ 0.15 MPa suction in the Venturi throat): this value represents the typical range of industrial compressed air supply. It generates sufficient suction to stabilize the flow field without excessive disturbance of the liquid, ensuring the practical feasibility of implementing the Venturi effect.

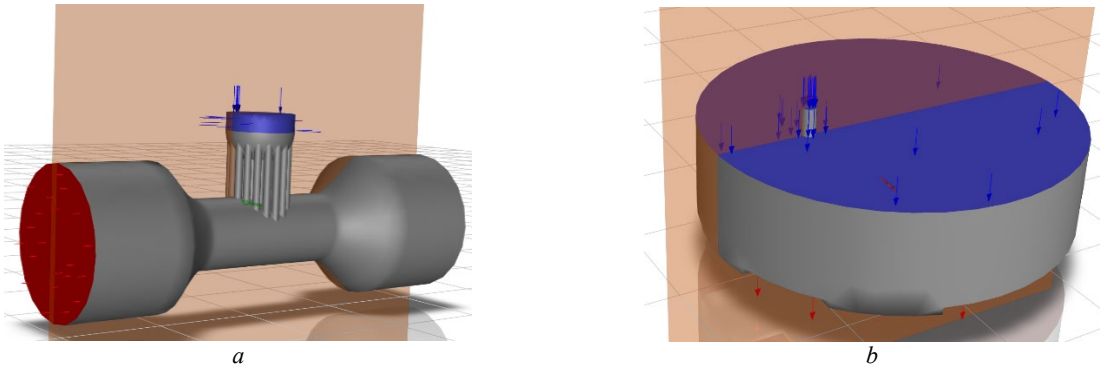

a *b*

Fig. 8. Numerical model and observation planes for the anti-splash design (*a*) and for the baseline design (*b*)

– Outlet (atmospheric pressure outlet): provides the natural discharge of the gas–liquid mixture, corresponding to the open environment of AWJM.

– Solid walls (no-slip boundary condition): constrain the sliding and breakup behavior of liquid films along surfaces, consistent with boundary layer theory.

The mesh was generated using an unstructured scheme with local refinement applied near the Venturi throat and the jet impact region to enhance resolution in areas of steep velocity gradients. Time discretization was explicitly controlled with a step of 2×10^{-6} s, maintaining the Courant number below 0.25 to ensure numerical stability and convergence. Transient states were selectively monitored at multiple time steps and processed in CFD-Post for analysis of velocity distributions and streamlines, thereby revealing how liquid splashes were dispersed and directed by suction forces.

For the quantitative evaluation of splash dispersion and velocity distribution in the domain, several observation planes were defined:

– Longitudinal plane: passes through the jet centerline and the entire cutting domain, capturing the full sequence from jet impingement to redistribution. This configuration reveals high-speed migration paths and gas–liquid interaction.

– Horizontal plane: positioned slightly above the bowl outlet, used to measure liquid volume fraction and droplet dispersion radius, providing direct assessment of vertical and radial dispersion.

– Baseline comparison plane: identical planes were placed in the control model to ensure comparability with the anti-splash protection structure. This setup guarantees that the numerical data directly correspond to experimental splash observations, enabling unambiguous validation.

3.3 Grid independence verification

To ensure that the results were not dependent on mesh resolution, a grid independence study was conducted. Three mesh density levels–coarse, medium, and fine–were tested, with evaluation of key parameters such as mixture velocity and water volume fraction at the observation planes. The results showed that after mesh refinement to approximately 1.2 million cells, the variation of these parameters was less than 2 %. Therefore, this mesh density was selected as the baseline configuration, balancing computational accuracy and efficiency. This process confirmed that the spatial discretization of the numerical model provides reliable results for subsequent analyses.

Discussion of simulation results and analysis of the splash suppression effect

Jet behavior during impingement.

Based on the methodology described above, the mixture velocity under steady-state conditions is analyzed. The mixture velocity represents the phase-weighted average of the local velocities of water and air, indicating the combined momentum transfer. The diagnostic principle is straightforward: if the mixture velocity is high while the water volume fraction is low, the momentum is dominated by air (e.g., near the throat). Conversely, if both parameters are high near the workpiece, droplets possess strong kinetic energy and tend to cause recontamination [21].

(a) Anti-splash design: bowl + Venturi (Fig. 9 *a*). Upon impingement, the jet attaches to the concave bowl, creating a wall-bounded sliding flow. The impact core is enveloped and redirected downward. As the flow enters the throat, the streamlines converge and accelerate, forming a stable suction-driven pathway where high-velocity regions are confined within the structure. The velocity contours along the workpiece surface display distinct “cold bands,” indicating a significantly reduced mixture velocity near the surface and suppressed tangential shear. Notably, the 0.7 peak contours do not spread above the working surface but are instead directed into the cavity, consistent with the anticipated “capture–guide–dissipate” mechanism.

(b) Baseline support (Fig. 9 *b*). Without geometric confinement or suction, the post-impingement jet generates a typical wall jet and strong shear layer. High-velocity regions accumulate near the processed surface and spread laterally across the span. Compared with Fig. 9 *a*, greater surface coverage by red/yellow zones indicates outward mo-

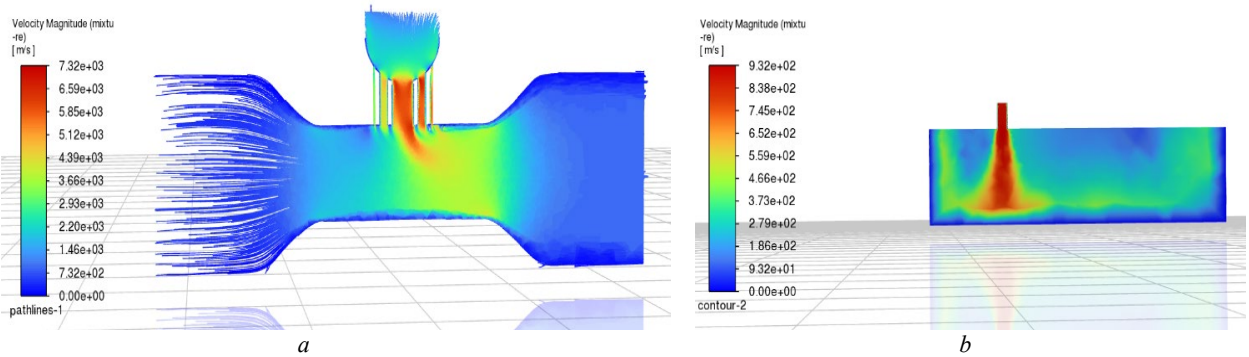

a *b*

Fig. 9. Velocity field and streamlines with the anti-splash structure (mixture phase) (*a*), and Velocity field and streamlines with the baseline structure (mixture phase) (*b*)

mentum leakage, which promotes droplet ejection and secondary rebound. Distinct recirculation cores also appear near the drainage holes, indicating unsteady capture–re-splash processes.

Thus, it can be stated:

– Shift in peak locations. In the anti-splash design, velocity peaks are drawn into the throat centerline; in the baseline case, they remain near the processed surface, indicating a shift in momentum pathways.

– Reduction of high-velocity coverage. With 0.7 peak contours, the anti-splash design exhibits much less surface coverage at high velocity, reducing the risk of shear and re-deposition.

– Suppressed recirculation. Large recirculation bubbles are absent in the anti-splash design but noticeable in the baseline case, where they contribute to upward entrainment.

It was further shown as follows.

The water volume fraction quantitatively reflects the concentration and dilution of the liquid, serving as a key indicator of the degree of splashing. Comparison of the two designs highlights differences in droplet formation, trajectory guidance, and deposition.

(a) Anti-splash design (Fig. 10 *a*). At the early stage, the bowl ensures film attachment and delays the breakup of bulges. Then the Venturi suction provides continuous downward entrainment, drawing the liquid into the throat until complete breakup. As a result, high-concentration zones remain confined inside the cavity, where droplets are diluted and dispersed. The volume fraction contours form a funnel-shaped constriction, confirming effective localization of splashing beneath the working zone.

(b) Baseline structure (Fig. 10 *b*) Without geometric confinement or suction, the film rapidly breaks into bulges and ejects large droplets. Directly above the working surface, a continuous band of high concentration develops, spreading into the open space and creating a risk of contamination beyond the processing zone. Radial dispersion is also greater, increasing the contamination region.

Thus, we have:

– Contrast of aggregation zones. Droplets cluster in the throat and cavity in the anti-splash design, whereas the baseline structure forms suspended high-density bands above the workpiece.

– Contrast in dilution velocity. Concentrations decrease rapidly from inlet to outlet in the anti-splash design, whereas the decrease occurs more slowly in the baseline case, indicating a prolonged droplet momentum.

– Contrast in dispersion degree. The height and radius of droplet dispersion are reduced by 30–40 % in the anti-splash design but extend beyond the cavity in the baseline case, causing wider contamination.

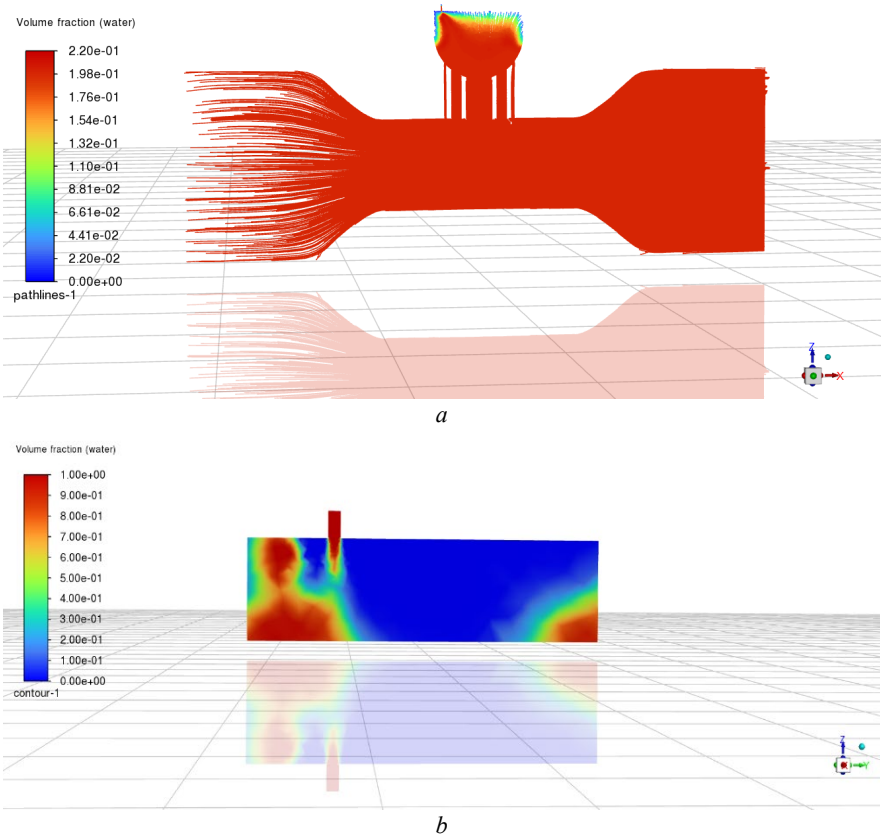

Fig. 10. Distribution of water volume fraction in the anti-splash design (*a*) and distribution of water volume fraction in the baseline structure (*b*)

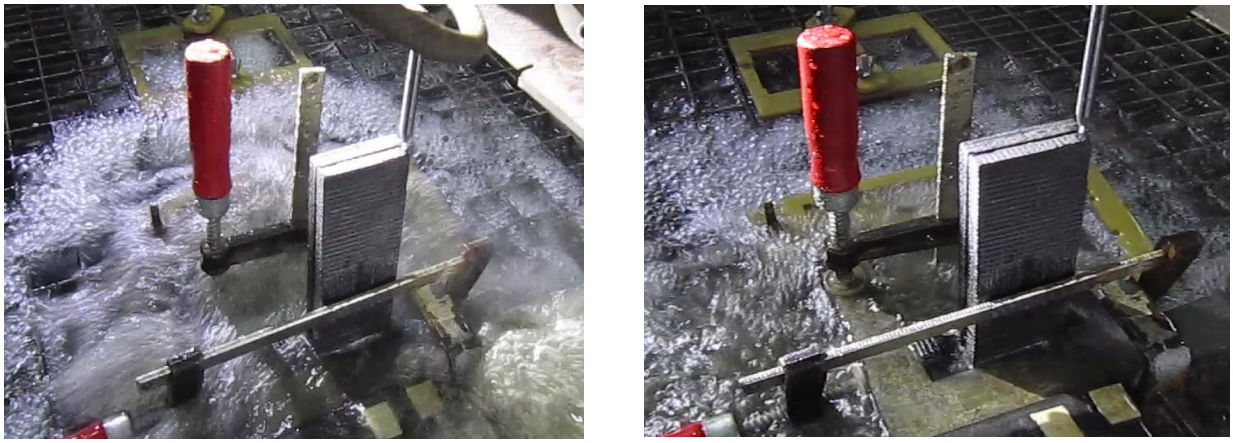

a *b*

Fig. 11. Cutting without the draining-flow splash suppression system (*a*) and with the system (*b*)

A comparative assessment and integration of velocity and concentration results lead to the following conclusions:

– Significant velocity suppression. In the anti-splash design, the peak mixture velocity near the liquid film is ≈35 % lower than in the baseline case, reducing the energy of upward droplets.

– Reduced contamination footprint. The droplet scattering height and radial range decrease by ≈40 % and 30 %, respectively, effectively limiting contamination.

– Shifted high-velocity zones. The baseline case shows high-velocity regions adjacent to the processed surface, creating a risk of secondary erosion; the anti-splash structure redirects them into the bowl and throat.

– Stabilized flow field. Streamlines are concentrated and aligned in the anti-splash design, reducing random splashing and uneven droplet formation.

Experimental verification demonstrated that when the ejection system is applied, splash reduction of the draining flow is achieved, especially at the moments when the jet enters or exits the workpiece, Fig. 11.

Overall, the proposed design demonstrates excellent performance in suppressing kinetic energy and limiting contamination. It not only improves the AWJM processing environment but also prevents secondary erosion of processed surfaces. This dual verification–through hydrodynamic mechanisms and numerical comparison–confirms the practical value of the design for industrial implementation.

Conclusions

This study addressed splash-induced contamination in abrasive water jet machining by proposing a structure with bowl confinement and Venturi suction. Simulation results confirmed that the design effectively suppresses upward ejection and diffusion of liquid splashes without compromising cutting efficiency. With this design, contamination footprints were significantly reduced, enhancing processing quality, extending equipment lifetime, and maintaining a clean working environment. These conclusions align with the trajectory of high-efficiency, clean, and precision manufacturing, while providing a validated engineering example of flow control under high-speed liquid influence.

Future studies should expand this concept to account for diverse fluid properties, flow rates, and spatial constraints. Lessons may be drawn from other fields: multiporous diffusers and guide-wall nozzles can attenuate local liquid momentum; gas curtain isolation from lithography may inspire droplet barriers in open environments [22]; and bottom-up filling strategies in the food industry may inform recovery of viscous liquids [23]. Through interdisciplinary integration and refinement, a universal framework for the design and evaluation of splash control in high-speed liquid environments may emerge, broadening industrial applicability and advancing the goals of high-quality and sustainable manufacturing.

Conflict of interest

The authors declare that they have no conflict of interest in relation to this research, including financial, personal, authorship, or any other nature that could affect the research and its results presented in this article.

Use of artificial intelligence

The authors confirm that they did not use artificial intelligence technologies when creating the current work.

References

[1] Y. Natarajan, P. K. Murugesan, M. Mohan and S. A. L. A. Khan, "Abrasive Water Jet Machining process: A state of art of review," *Journal of Manufacturing Processes*, Vol. 49, pp. 271–322, Jan. 2020, doi: https://doi.org/10.1016/j.jmapro.2019.11.030.

[2] T. Nguyen and J. Wang, "A review on the erosion mechanisms in abrasive waterjet micromachining of brittle materials," *International Journal of Extreme Manufacturing*, 1(1), 012006, 2019, doi: https://doi.org/10.1088/2631-7990/ab1028.

[3] V. K. Mahakur, S. Bhowmik and P. K. Patowari, "Machining parametric study on the natural fiber reinforced composites: A review," *Proceedings of the Institution of Mechanical Engineers Part C Journal of Mechanical Engineering Science*, Vol. 236(11), pp. 6232–6249, 2021, doi: https://doi.org/10.1177/09544062211063752.

[4] Y. D. Chashechkin and A. Y. Ilinykh, "Multiple Emissions of Splashes upon Drop Impact," *Doklady Physics*, Vol. 65(10), pp. 366–370, 2020, doi: https://doi.org/10.1134/s1028335820100067.

[5] M. Rein, "Phenomena of liquid drop impact on solid and liquid surfaces," *Fluid Dynamics Research*, Vol. 12(2), pp. 61–93, 1993, doi: https://doi.org/10.1016/0169-5983(93)90106-k.

[6] J. Liu et al., "Splashing phenomena during liquid droplet impact," *Atomization and Sprays*, Vol. 20(4), pp. 297–310, 2010, doi: https://doi.org/10.1615/atomizspr.v20.i4.30.

[7] Y. Qian et al., "Experimental study on the kerf characteristic and cross-section quality of CFRP laminates cut by steel slag abrasive waterjet," *The International Journal of Advanced Manufacturing Technology*, Vol. 137, pp. 2547–2562, 2025, doi: https://doi.org/10.1007/s00170-025-15297-1.

[8] M. Li et al., "Study on kerf characteristics and surface integrity based on physical energy model during abrasive waterjet cutting of thick CFRP laminates," *The International Journal of Advanced Manufacturing Technology*, Vol. 113(1–2), pp. 73–85, 2021, doi: https://doi.org/10.1007/s00170-021-06590-w.

[9] M. Du et al., "Advanced waterjet technology for machining beveled structures of High-Strength and thick material," *Machines*, Vol. 12(6), 408, 2024, doi: https://doi.org/10.3390/machines12060408.

[10] R. Kodandappa et al., "Application of the Taguchi method and RSM for process parameter optimization in AWSJ machining of CFRP composite-based orthopedic implants," *Open Engineering*, Vol. 14(1), 2024, doi: https://doi.org/10.1515/eng-2024-0057.

[11] I. A. Popan et al., "Artificial intelligence model used for optimizing abrasive water jet machining parameters to minimize delamination in carbon Fiber-Reinforced polymer," *Applied Sciences*, Vol. 14(18), 8512, 2024, doi: https://doi.org/10.3390/app14188512.

[12] K. Vijayananth et al., "An integrated CRITIC-COPRAS approach for multi-response optimization on AWJM of hybrid filler–reinforced polymer composite and its surface integrity," *The International Journal of Advanced Manufacturing Technology*, Vol. 131(9–10), pp. 4965–4980, 2024, doi: https://doi.org/10.1007/s00170-024-13267-7.

[13] Y. Zhang, et al., "A novel quantitative analysis approach for hole surface damage of ceramic matrix composites machined by abrasive waterjet", *Journal of Manufacturing Processes*, Vol. 108, pp. 217–226, 2023, doi: https://doi.org/10.1016/j.jmapro.2023.11.012.

[14] D. Shanmugam, T. Nguyen and J. Wang, "A study of delamination on graphite/epoxy composites in abrasive waterjet machining," *Composites Part A: Applied Science and Manufacturing*, Vol. 39(6), pp. 923–929, 2008, doi: https://doi.org/10.1016/j.compositesa.2008.04.001.

[15] S. Jani et al., "Design and optimization of unit production cost for AWJ process on machining hybrid natural fibre composite material," *International Journal of Lightweight Materials and Manufacture*, Vol. 4(4), pp. 491–497, 2021, doi: https://doi.org/10.1016/j.ijlmm.2021.07.002.

[16] J. Chen et al., "Analytical modeling of effective depth of cut for ductile materials via abrasive waterjet machining," *The International Journal of Advanced Manufacturing Technology*, Vol. 124(5–6), pp. 1813–1826, 2022, doi: https://doi.org/10.1007/s00170-022-10538-z.

[17] J. Chen et al., "Smoothing strategy for corner of small curvature radius by abrasive waterjet machining", *Advances in Manufacturing*, Vol. 11(3), pp. 390–406, 2023, doi: https://doi.org/10.1007/s40436-023-00443-3.

[18] M. Hashish, "Optimization factors in Abrasive-Waterjet machining," *Journal of Engineering for Industry*, Vol. 113(1), pp. 29–37, 1991, doi: https://doi.org/10.1115/1.2899619.

[19] H. Wang et al., "Research progress in abrasive water jet processing technology," *Micromachines*, Vol. 14(8), 1526, 2023, doi: https://doi.org/10.3390/mi14081526.

[20] O. Salenko et al., "Using a functional approach in solving problems improve performance waterjet equipment," *Problems of tribology*, Vol. 27(2/104), pp. 94–103, 2022, doi: https://doi.org/10.31891/2079-1372-2022-104-2-94-103.

[21] Q. Deng, A. V. Anilkumar and T. G. Wang, "The role of viscosity and surface tension in bubble entrapment during drop impact onto a deep liquid pool," *Journal of Fluid Mechanics*, Vol. 578, pp. 119–138, 2007, doi: https://doi.org/10.1017/s0022112007004892.

[22] B. J. Lin, "Immersion lithography and its impact on semiconductor manufacturing," *Journal of Micro/Nanolithography MEMS and MOEMS*, Vol. 3(3), 377, 2004, doi: https://doi.org/10.1117/1.1756917.

[23] W. Kim, J. Eun and S. Jeon, "Anti-splashing properties of sticky superhydrophobic surfaces," *Applied Surface Science*, Vol. 542, 148617, 2020, doi: https://doi.org/10.1016/j.apsusc.2020.148617.

Утримання стікаючого водоабразивного потоку засобами уловлення струменя для захисту від бризок зворотної крайки заготовки

Сяньдін Сюе[1] • **О. Ф. Саленко**[1]

[1] *КПІ ім. Ігоря Сікорського, Київ, Україна*

Анотація: *Абразивна гідроструминна обробка (AWJM) широко використовується в аерокосмічній та прецизійній виробництві завдяки своїй природі холодного різання. Однак залишковий стовп високоенергетичного струменя, що проникає в заготовку, часто впливає на опорну конструкцію, створюючи інтенсивне розбризкування, яке призводить до забруднення поверхні та вторинних пошкоджень. Щоб вирішити цю проблему, ми пропонуємо оригінальну опорну конструкцію, що запобігає розбризкуванню, що поєднує увігнуту поверхню чаші з механізмом негативного тиску, індукованим Вентурі. Використовуючи багатофазне моделювання VOF у поєднанні з перевіркою розрахунків методом кінцевих елементів, з'ясовано синергетичний механізм керування: вигнута чаша сприяє ковзанню рідини, що прилягає до стінки, для зменшення радіального імпульсу, тоді як горловина Вентурі створює зону негативного тиску ~0,15 МПа, яка захоплює краплі в канал нижче за течією для розсіювання. Результати досліджень довели, що порівняно зі звичайними опорами, конструкція зменшує пікову швидкість суміші на ~35 %, зменшує висоту дифузії крапель на 40 % та зменшує радіальне розсіювання на 30 %, ефективно обмежуючи зони забруднення. Статистичний аналіз додатково підтверджує, що конструкція підтримує високі запаси міцності навіть за екстремальних навантажень. Ці результати не лише покращують середовище обробки абразивним гідроструминним струменем (AWJM), але й забезпечують нове рішення задачі для високошвидкісного контролю взаємодії рідини. У майбутньому цей механізм резонує з потребами придушення бризок у фотолітографії, упаковці харчових продуктів, електронній інкапсуляції та різанні металу, прокладаючи шлях для універсальної системи проектування та оцінки контролю бризок у передовому виробництві.*

Ключові слова: *абразивна гідроструминна обробка; придушення бризок; ефект Вентурі; чисельне моделювання; взаємодія рідини та поверхні.*